ISSN 0016-8521, Geotectonics, 2019, Vol. 53, No. 1, pp. 125–139. © Pleiades Publishing, Inc., 2019.

Microstructural Study and Strain Analysis of Deformed Neoproterozoic Lithologies in the Um Junud Area, Northern Nubian Shield[1]

Osama M. K. Kassem[a, b, *], Z. Hamimi[c], H. Aboelkhair[d], A. Abdelhalim[e], and M. Al-Gabali[f]

[a] *King Saud University, Faculty of Science, Department of Geology – SGSRC, P.O. Box 2455, Riyadh, 11451 Saudi Arabia*

[b] *National Research Center, Geology Department, Dokki, Cairo, 12622 Egypt*

[c] *Benha University, Geology Department, Faulty of Science, Qalubiya Governorate, Benha, 13511 Egypt*

[d] *Damietta University, Geology Department, Faculty of Science, New Damietta, Egypt*

[e] *Cairo University, Department of Geology, Faulty of Science, Giza, Cairo, 12613 Egypt*

[f] *Thamar University, Department of Environmental and Earth Sciences, Dhamar, Yemen*

**e-mail: kassemo1@yahoo.com*

Received February 26, 2018; Revised June 7, 2018; Accepted September 25, 2018

Abstract—Estimation of finite strain and microstructural analysis of deformed rocks are keys to better understanding deformational processes and related structures in a variety of scales started from microscopic fabric development to regional-scale structures. In the present work, we carried out the quantitative calculation of strain using the R_f/φ and Fry methods for quartz, feldspar and mafic grains (e.g. biotite and hornblende) from twenty two collected samples for granitic gneiss, amphibolite and hornblende schist samples from the Um Junud area situated in south Eastern Desert of Egypt. Forty four thin sections were prepared and measured by using finite strain methods. The strain data indicate high to moderate ranges of deformation of the amphibolite to granitic rocks. The axial ratios in the XZ section range from 1.74 to 4.37 and 1.50 to 4.46 for the R_f/φ and the Fry methods respectively. The finite strain direction for the long axes displays clustering along N to WNW trend, and shallow WNW plunging in the majority of the studied samples. The short axes are found to be subvertical associated with a subhorizontal foliation. It is concluded that finite strain is of the same order of magnitude for various lithologic units outcropping in the area, and that contacts were formed under semi-brittle to semi-ductile deformation conditions. Thus, the finite strain accumulated during superimposed deformation on a previously nappe structure assemblage, which pointed out that these contacts were created during the accumulation of finite strain. This result is inconsistent with the generally believed that nappe creation in orogens carried out by simple shear deformation.

Keywords: microstructural study, finite strain, Neoproterozoic lithologies, Eastern Desert, Egypt

DOI: 10.1134/S0016852119010023

INTRODUCTION

Many authors are conventional that the East African Orogen (EAO) in the Eastern Desert of Egypt was consolidated in the Neoproterozoic by accretion of island arcs [14, 33, 22]. In the Arabian-Nubian Shield, the Neoproterozoic rocks are exposed in the Eastern Desert of Egypt as a result of the Red Sea rift [33, 22]. The Eastern Desert (ED) is divided into the structural basement and structural cover as major tectonostratigraphic units (Fig. 1). The structural basement includes gneisses and related amphibolites rocks [9, 24]. Furthermore, the structural cover (Pan African nappes) consists of low-grade metamorphosed ophiolite slices (such as pillow lavas, serpentinites and metagabbros) and metavolcano-sedimentary rocks [37, 12]. The Pan African nappes were strongly deformed during oblique collision of the island arcs with accretion onto the Saharan Metacraton creating an ophiolitic mélange [4]. Consequently, the development of the Najd Fault System was resulted in its NW-trending and sinistral shear zones [11, 1–3].

More studies in the Eastern Desert (ED) deal with Northern Eastern Desert (NED) and Central Eastern Desert (CED), while the Southern Eastern Desert (SED) has been less studied. That is reflected onto the Tectonic scenarios that suggested to the SED which seems to generally represent a deeper level of exposure than the CED and was less affected by Najd shearing [33]. The Um Junud area is located in the SED and has variety in Neoproterozoic basement rocks and structures. It is a key area for understanding the tectonic evolution of the SED. During the late Proterozoic several suites of volcanic and volcanoclastic rocks with island arc affinities, granitoid plutons and ophi-

[1] The article is published in the original.

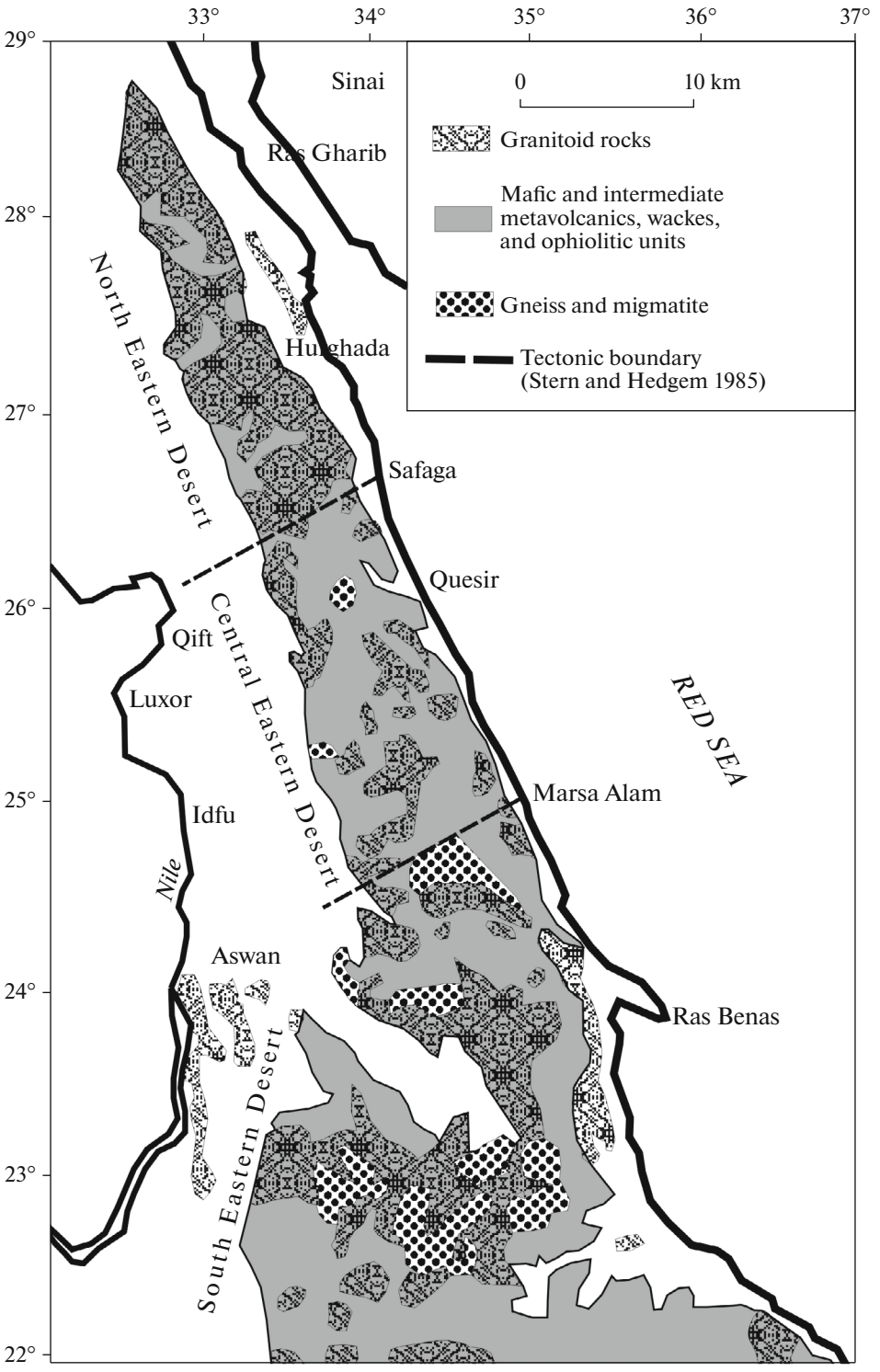

Fig. 1. Geological sketch map for the Eastern desert of Egypt (modified [34]).

olitic blocks were welded together to form a thick continental crust prior to their accretion onto the ancient African Craton [13, 7, 14, 31, 5, 16].

In the present work, we are using the finite strain measurements to determine the magnitude and orientation of the finite strain ellipsoid which is considered the principal goals of microstructural geology. For example, it is an important role to investigate the displacement across ductile shear zones including fold and fault mechanisms, and volume changes during

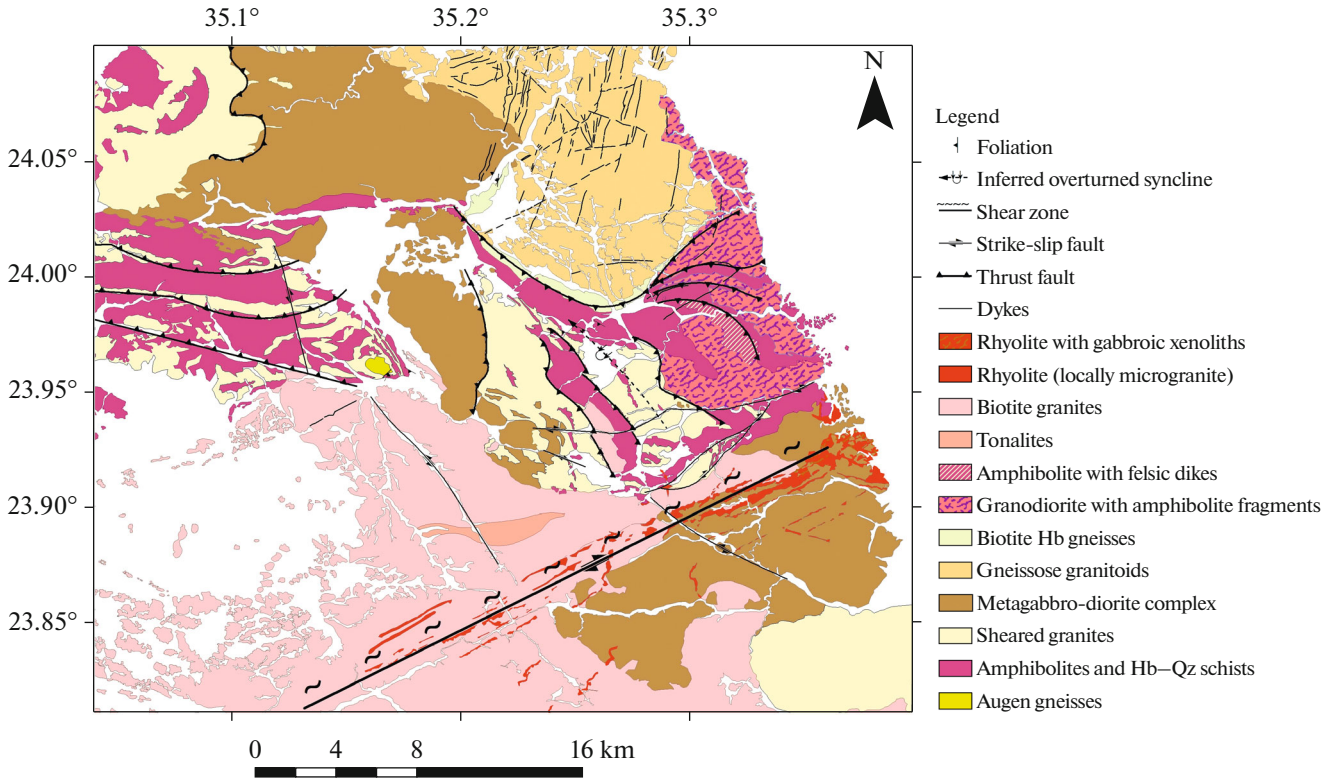

Fig. 2. Geological map of the Um Junud area.

deformation. Most strain measurement techniques are useful such as reduction spots, R_f/ϕ, center-to-center, Fry methods. The finite strain ratios were measured by many applications [20, 17, 18]. However, some applications for absolute finite strains are required. Measurement of finite strains help to detect the objects of pre-deformation form whereas strain ratios may be determined if rocks contain objects of known shape or distribution. In this work, we used the strain technique to realize the deformed rocks. The current work focuses on the finite strain, strain variation patterns and microstructural analysis for the Um Junud area. Using these data, we estimate the nature, distribution of strain and mechanical behavior of the faults and tectonic setting during deformation in the Um Junud area.

GEOLOGICAL SETTING

The exposed lithologic units in the area are arranged in a chronologic order from oldest to youngest as follows: Augen Gneisses, Amphibolites and Hornblende-Quartz Schist, Sheared granites, Metagabbro-Diorite Complex, Gneissose granitoids, Granodiorite with amphibolite Fragments, Tonalite, Biotite granite, Perthitic leucogranite, Rhyolite and microgranite, and dykes (Fig. 2).

The augen gneisses occur as a relatively small outcrop in the southern continuation of Jabal Abu Jurdi (Fig. 3a). They have a granoblastic texture of sutured, mosaicked and stretched-out granulated quartz masses which are represented quartz ribbons in the augen gneisses. The amphibolites and hornblende-quartz schist are cropping out at the central eastern and western parts of the study area. The amphibolites are gray to dark gray in color, fine-grained to coarse-grained and in some places they are characterized by a conspicuous schistosity resulted from subparallel alignment of hornblende, plagioclase and biotite (Fig. 3b). They are sheared, brecciated, cataclased and occasionally partly migmatized. The sheared granites outcrop in several locations in the mapped area. They are showing preferred orientation of quartz and feldspar minerals. In Nasb Eiqat and Jabal Um Junud, they show massive appearance, whearas in Jabal Um Dalaq and to the west of Wadi Abu Diban and Wadi Na'ait become more sheared, and in Jabal Abu Jurdi appear remarkably foliated. The metagabbro-diorite complex rocks have a massive texture and a distinguished spheroid weathering. In Jabal Almandeet, they are intruded by rhyolite (Fig. 3c), and in Jabal Lahami are traversed by mafic dykes, and in places they are injected by quartz veins.

The gneissose granitoids are encountered at the northeastern part of the study area forming Jabal Alhefery. These rocks have an oval outcrop area and locally form a low to relatively moderate relief country. They are jointed and dissected by basic dykes which mainly trend in the N-S to NNE-SSW directions.

They are exfoliated and include xenolithic enclaves, which were foreign bodies captured from the surrounding country rocks by the igneous protolith of the gneissose granitoids. The contacts between the gneissose granitoids and surrounding lithologies are intensively sheared and have subvertical foliations (Fig. 3d). The granodiorite with amphibolite fragments are encountered in Jabal Al-Sweekhy and Jabal Abu Marwah. The amphibolite fragments often show a sigmoidal pattern and their arrangement reflects shearing in the NW-SE direction (Fig. 3e). They are jointed and intruded by mafic dykes dipping toward eastward. The tonalite is exposed in the southern continuation of Wadi Albeday and Wadi Shorok. In the ASTER image, the tonalite outcrop area shows a sigmoidal shape with distinctive color inside the enveloping biotite granite. The biotite granite occupies a vast domain in the southern part of the mapped area. The rock is medium to coarse grained, gray in color, massive and exhibits exfoliations (Fig. 3f). It consists of plagioclase, microcline, quartz, biotite and hornblende. Kaolinite and epidote are secondary minerals. The perthitic leucogranite is encountered as unmapable masses at Jabal Almandeet (Fig. 3g).

The rhyolite and microgranite are cropping out in the southeastern part of the mapped area in the form of dyke swarms. The study area was traversed by numerous basic dykes. The most prominent dykes are in the northeast of the study area, where Dyke swarms extend to few kilometers. They are trending in various directions but are commonly orientated in two major directions NNE-SSW and ENE-WSW. In many cases, the dykes are fractured, with remarkable epidotization along dyke. It is observed that the effect of weathering for some dykes is lesser than that the country rocks, which led to creating well developed ridges which stand out in relief.

METHODOLOGY

The samples preparation for microstructural investigation and finite strain analysis involved cutting thin sections samples along three perpendicular faces parallel the XY, YZ and XZ principal planes. The felsic minerals (such as k-feldspar, plagioclase and quartz) and mafic minerals were scanned and digitized. Some programs were used to calculate deformed digitized ellipse and to detect its orientation and relative position. The Um Junud and adjacent areas have been investigated by collecting samples from different types of rocks. Thin sections of representative samples from the Um Junud area were examined using a polarized microscope to find out the mineral composition and textures, and to clarify effects of deformation, alteration and metamorphic grade of these rocks.

In the present work, we depend on the THETA program for the R_f/ϕ method and the FRY programs for fry method to measure strain parameters which were described by [27]. Furthermore, for calculation and plotting strain data, we used EllipseFit program with using different parameters, simulated pure shear, simple shear, and general shear. For R_f/ϕ analysis, we measured along the long and short axes for feldspar and mafic ellipsoids up to 50 grains per polished slabs and/or thin sections and also calculated the mean aspect ratio for different ellipsoids for each section. [26] suggested that the deformation and shape of the feldspars and mafic minerals depend on metamorphic conditions. The deformation for feldspars grains is characherized at low metamorphic grade by brittle fracturing and cataclastic flow and at high metamorphic grade by ductile deformation. Tectonic strains were described by the chi-squared minimum of the R_f/ϕ techniques [27]. The central points of feldspar and mafic grains were applied to compute strain for the Fry analysis. The estimation of strain was performed by calculating the strain ellipsoid along the modified least-square technique of [25].

During the field trips, twenty two samples were collected from granite, granitic gneiss, amphibolite and hornblende schist samples in the Um Junud area (Fig. 4). The microstructural analysis was performed for the following rocks: 1 granite, 1 sheared granite, 2 gneiss, 1 granitic gneiss, 11 amphibolite and 6 hornblende schist samples. Feldspar (such as plagioclase), quartz, chlorite and hornblende were analysed by investigation of thin sections to see whether the deformation history is recorded in the hornblende schist and amphibolite rocks. In addition, the strain magnitude parameter is the same in the different type of rocks in the studied area (Fig. 4).

MICROSTRUCTURE AND DEFORMATION

In the present work, polished slabs and thin sections of representative samples were prepared for mesostructural and microstructural studies. The prepared samples were cut through the XY, XZ and YZ axes planes using both foliation and lineation [21]. We also carried out a mineralogical study of samples collected from deformed rocks. The meta-granite is display medium to coarse grained, gray in color, massive,

Fig. 3. (a) Lens displaying the sigmoidal structure with the monoclinic symmetry in an augen gneiss. (b) Field photograph showing shared granite and amphibolite schist in western Wadi Na'ait. Looking SW. (c) Microgranitic and rhyolitic intrusions within the metagabbro of Wadi Almandeet. Looking WNW. (d) Subvertical foliation near the outer margins of the gneissose granitoids in Wadi Lahmi. Looking E. (e) Field photograph showing sigmoidal amphibolite fragments within a granodiorite, Wadi Na'ait. Looking S. (f) Field photograph showing an exfoliated biotite granite. Wadi Albeday. Looking NE. (g) Field photograph showing an outcrop of a perthitic leucogranite along the flanks of Wadi Almandeet. Looking NW.


(a)
(b)
(c)
(d)
(e)
(f)
(g)

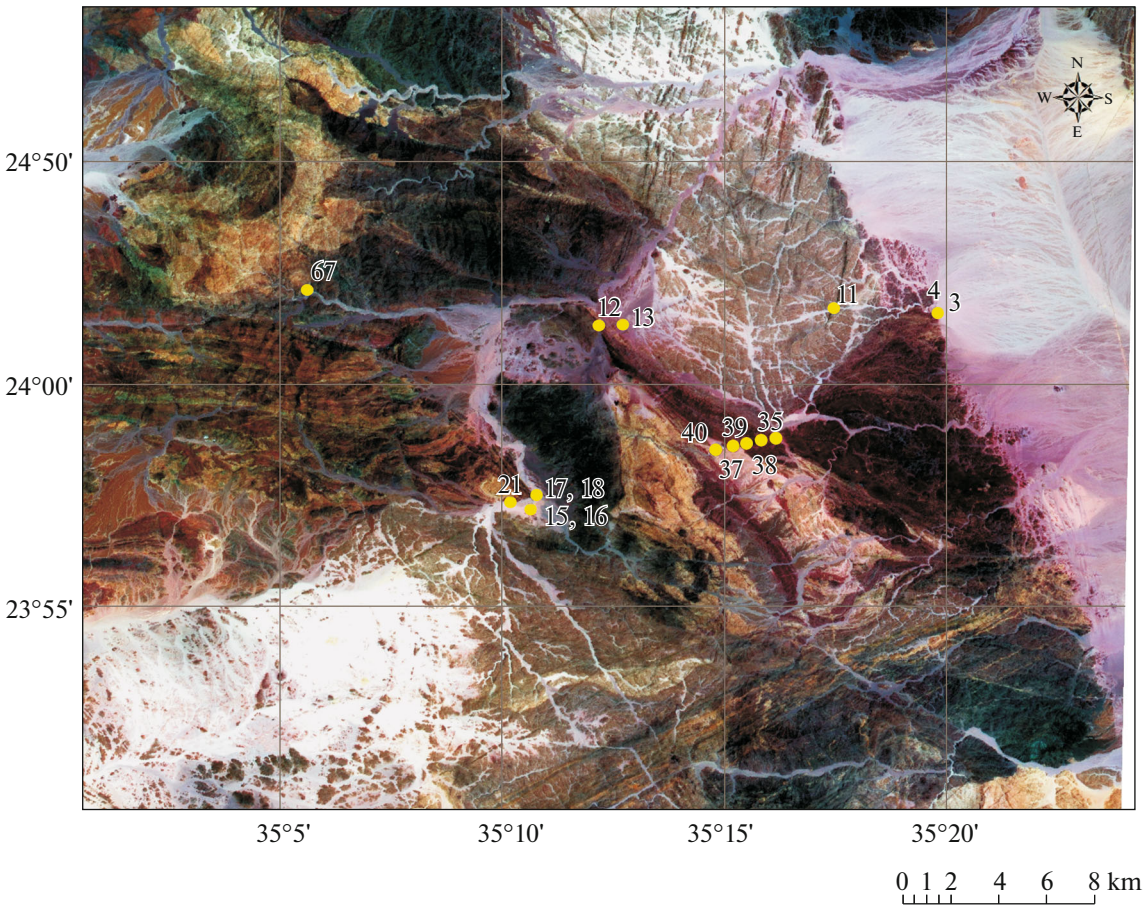

Fig. 4. Landsat map showing the sample location.

exhibits exfoliations and weakly deformed (Fig. 5a). Microscopically, it consists of plagioclase, microcline, quartz, biotite and hornblende. Kaolinite and epidote are secondary minerals. The microgranite occurs in the southeastern part of the mapped area in the form of dyke swarms. These dyke swarms are related to shear zones, and are oriented in the ENE-WSW. The rock is pink to red in color is occasionally sheared and trends in the NE direction with nearly vertical dip. The microgranite is fine-grained, pink in color and is highly sheared (Fig. 5b). Microscopically, quartz, orthoclase and plagioclase are the main components. The rock shows well developed spherulitic texture and foliated (Fig. 5b). When grain size is coarser (microgranite), it shows myrmekite texture due to the intergrowth between quartz and plagioclase. In some thin sections, perthitic texture between plagioclase and K-feldspar is observed.

The gneissose granitoids are characterized by exfoliated and include xenolithic enclaves. The contacts between the gneissose granitoids and surrounding lithologies are intensively sheared, moderately deformed and have subvertical foliations (Fig. 5c). Microscopically, the gneissose granitoids consist of plagioclase, quartz, hornblende and biotite. Secondary minerals are epidote, chlorite. Opaques are accessories (Fig. 5c). The gneisses have a granoblastic texture of sheared, mosaicked and stretched-out granulated quartz ribbons with deformed granites. They are composed essentially of plagioclase, quartz, biotite, microcline and hornblende. The largest, most distinct eyes are generally plagioclase and quartz. The gneisses are fine-grained to medium-grained, gray to light pink in color, with noticeable mica flakes and medium to high deformation (Fig. 5d).

The sheared granites are alternated with the amphibolites. These rocks are of pale brown color, fine- grained to medium-grained and show a preferred orientation of quartz and feldspar minerals. They show a massive appearance with foliated (see Figs. 5e, 5f). Microscopically, the sheared granites consist of quartz, K-feldspars (microcline and orthoclase), plagioclase, hornblende and muscovite. Epidote and chlorite of penninite variety are secondary minerals. These constituents are occasionally mylonitized and quartz crystals are frequently highly strained showing a strong undulatory extinction (Figs. 5e, 5f). Bending, kinking and crumpling of plagioclase along with broken K-feldspars are rather evidence supporting a cataclastic effect (Figs. 5e, 5f).

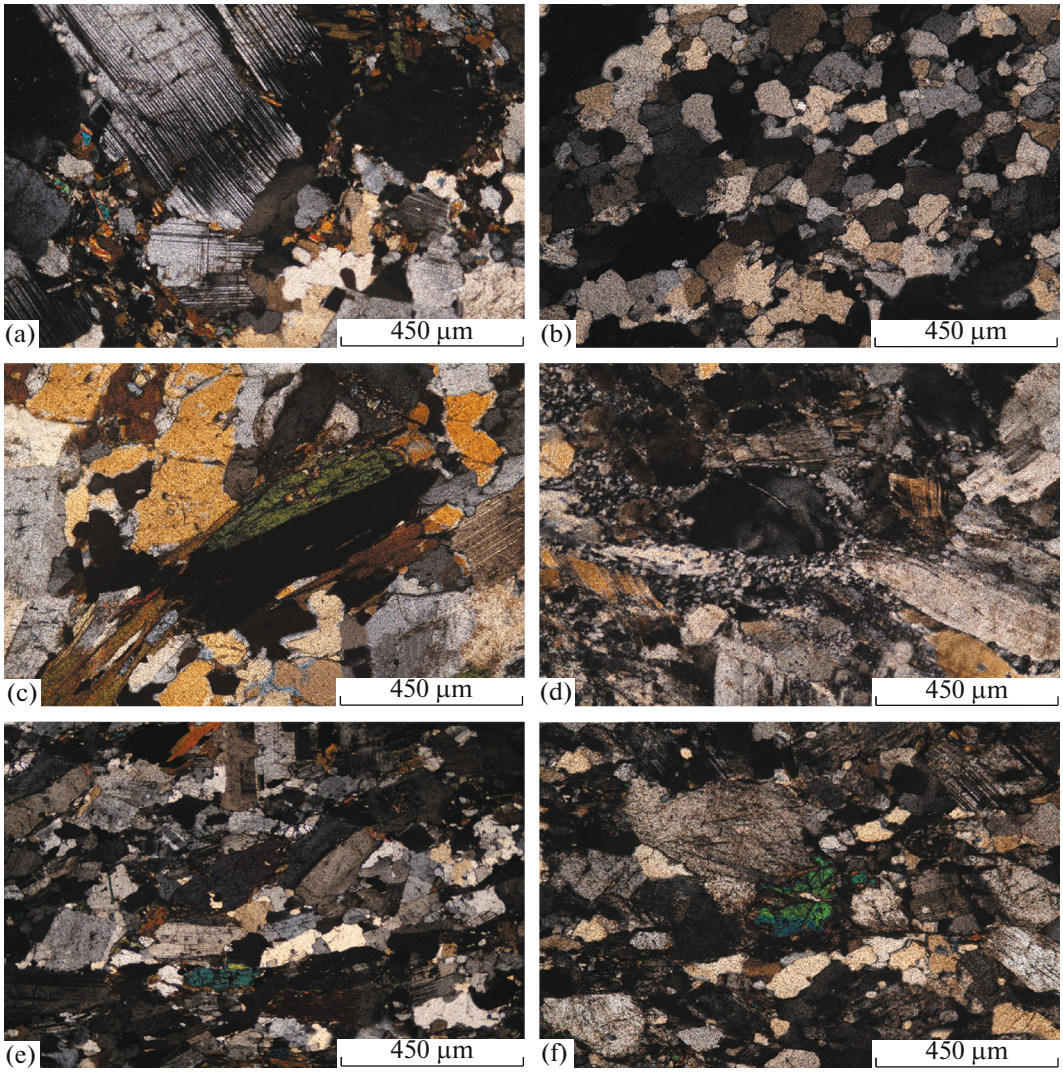

Fig. 5. Microphotographs of: (a) Weakly deformed granitic rock composed of plagioclase, quartz, and biotite (Sample S12); (b) Microgranite characterized by fine grains and slight to moderate shearing (Sample S16); (c) Well foliated and sheared gneissose granitoid (Sample S4). (d) Foliated and highly deformed gneiss showing elongated feldspars (Sample S11); (e) Sheared granitic rock displaying highly elongated potash feldspars (Sample S6); (f) Highly sheared granitic sample (Sample S6).

The amphibolites occur as alternated bands and layers with the sheared granites (Figs. 6a, 6b, 6c). The amphibolites are gray to dark gray in color, fine-grained to coarse-grained and in some places they are characterized by a conspicuous schistosity resulted from a subparallel alignment of hornblende, plagioclase and biotite (Figs. 6a, 6b, 6c). They are sheared, brecciated, cataclased and occasionally partly migmatized. The amphibolites are intruded by granite, invaded by quartz veins and traversed by mafic dykes and veinlets cutting across sheared varieties (Figs. 6a, 6b, 6c).

Microscopically, the amphibolites rocks consist of preferably lineated crystals of hornblende, quartz and plagioclase, with calcite, epidote and opaques minerals (Figs. 6a, 6b, 6c). The hornblende-quartz schists are characterized by fine grains and mylonitized textures (Figs. 6d, 6e, 6f). They display a banding parallel to the gneissosity (Figs. 6d, 6e, 6f). Mica is associated with hornblende and exists as subidiomorphic flakes arranged subparallel to the main planar fabric.

STRAIN MEASUREMENTS

The locations of studied samples for strain analysis of granitic gneiss, hornblende schist and amphibolite samples in the Junud area are displayed in Fig. 3. Our strain data demonstrate that the long axes in granitic gneiss rocks in the Um Junud area trend West/West-North-West to West/West-South-West and gently plunges of about 16° (Fig. 7a). The intermediate Y axes shallowly plunge to West/West-South-West and East/East-North-East and shallow plunges of about 8° (Fig. 7b). The short Z axes steeply plunge South-

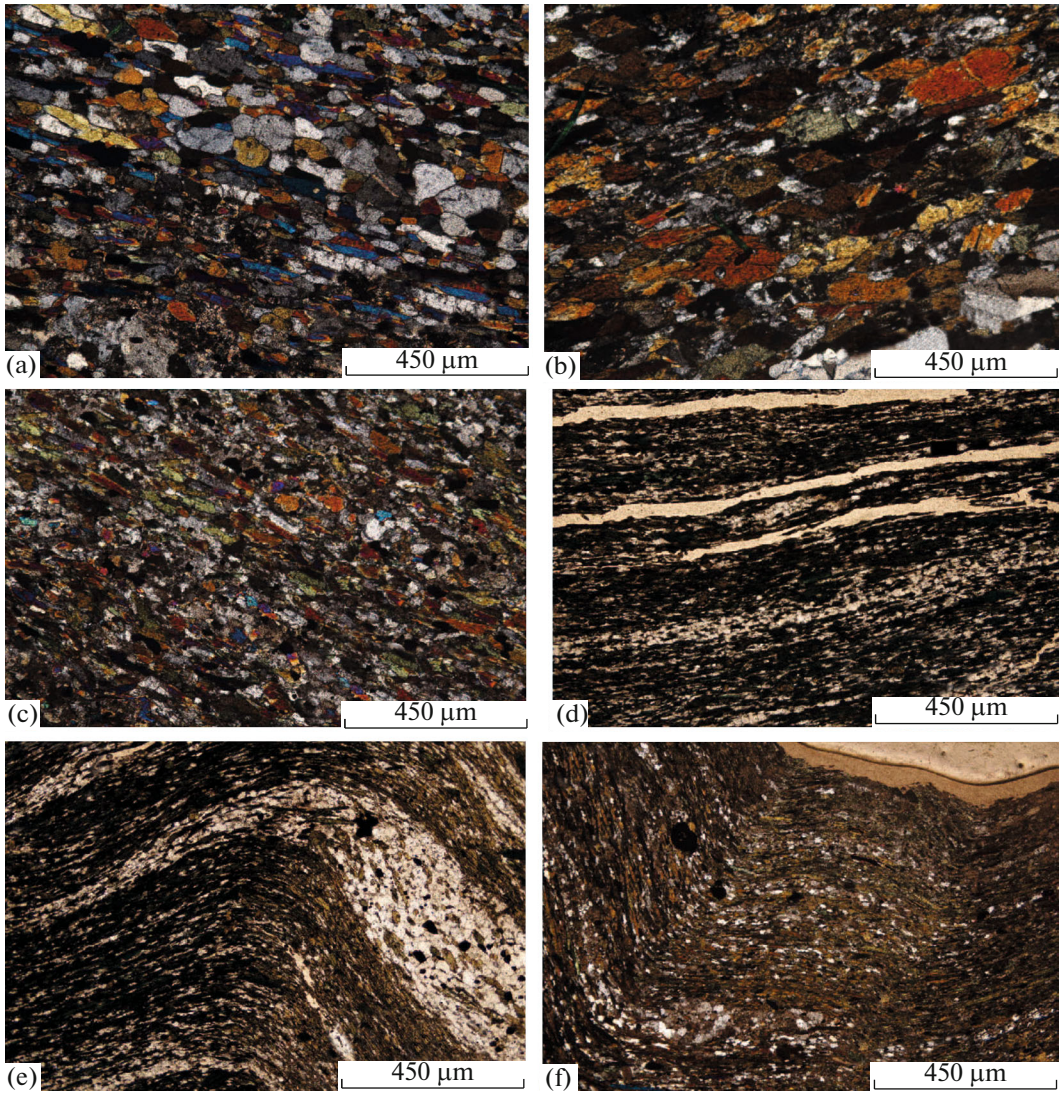

Fig. 6. Microphotographs of: (a) Amphibolite displaying linear aggregates of hornblende (Sample S3); (b) Amphibolite consisting fundamentally of preferably oriented crystals of hornblende (Sample S18); (c) Amphibolite (Sample S21); (d) Hornblende-quartz schist showing alternated bands and layers (Sample S35); (e) Fine-grained hornblende-quartz schist are characterized by fine grains and mylonitized textures (Sample S40); (f) Hornblende-quartz schist are characterized by rootless intrafolial folds (Sample S34).

East with about 66° (Fig. 7c). As a result, the mean of short Z axes is associated with vertical to subvertical and a horizontal to subhorizontal foliation.

The gneisses rocks are composed of quartz, feldspar, hornblende and mica which are four mechanically different mineral phases. The deformation behaviour of K-feldspar and plagioclase is rather similar with some difference [26]. In other case, the deformation behaviour of mafic minerals (biotite and hornblende) is dissimilar to that of the felsic grains (K-feldspar and plagioclase). For example, quartz is the strongest mineral. The studied samples display that no major difference in deformation behaviour of the feldspar porphyroclasts, amphibole minerals, and the quartz-mica matrix are observed. In addition, the investigated samples were undergone by a higher metamorphic grade and display a similar deformation of the same magnitude. Thus, the foliation of the main deformation phase recorded in granitic gneisses, hornblende schists and amphibolite samples with comparing to each other, which shows a similar deformation behaviour in all different types of rocks (Figs. 8, 9).

The measured finite strain data are briefed in the Table and also plotted in a Flinn diagram [10] in Fig. 10. Furthermore, the relationship between prolate and oblate shapes of the strain ellipsoids is an important information to assume strain type, for example constrictional or flattening deformation. In measured samples, their strain symmetry is characterized by oblate strain ellipsoids (Fig. 10). The axial ratios calculated by R_f/ϕ technique the in XZ sections range from 1.74 to 4.37 with S_X ranging from 1.22 to 1.77

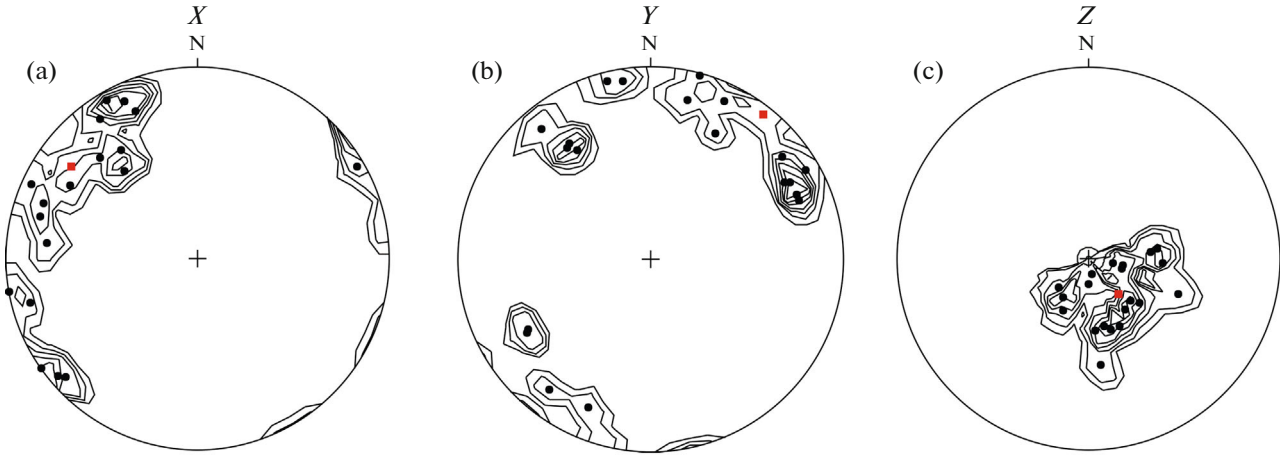

Fig. 7. Lower-hemisphere equal-area projections: (a) maximum extension axis (X), (b) intermediate axis (Y), (c) maximum shortening axis (Z). Contours start at 1% and increment every 3%.

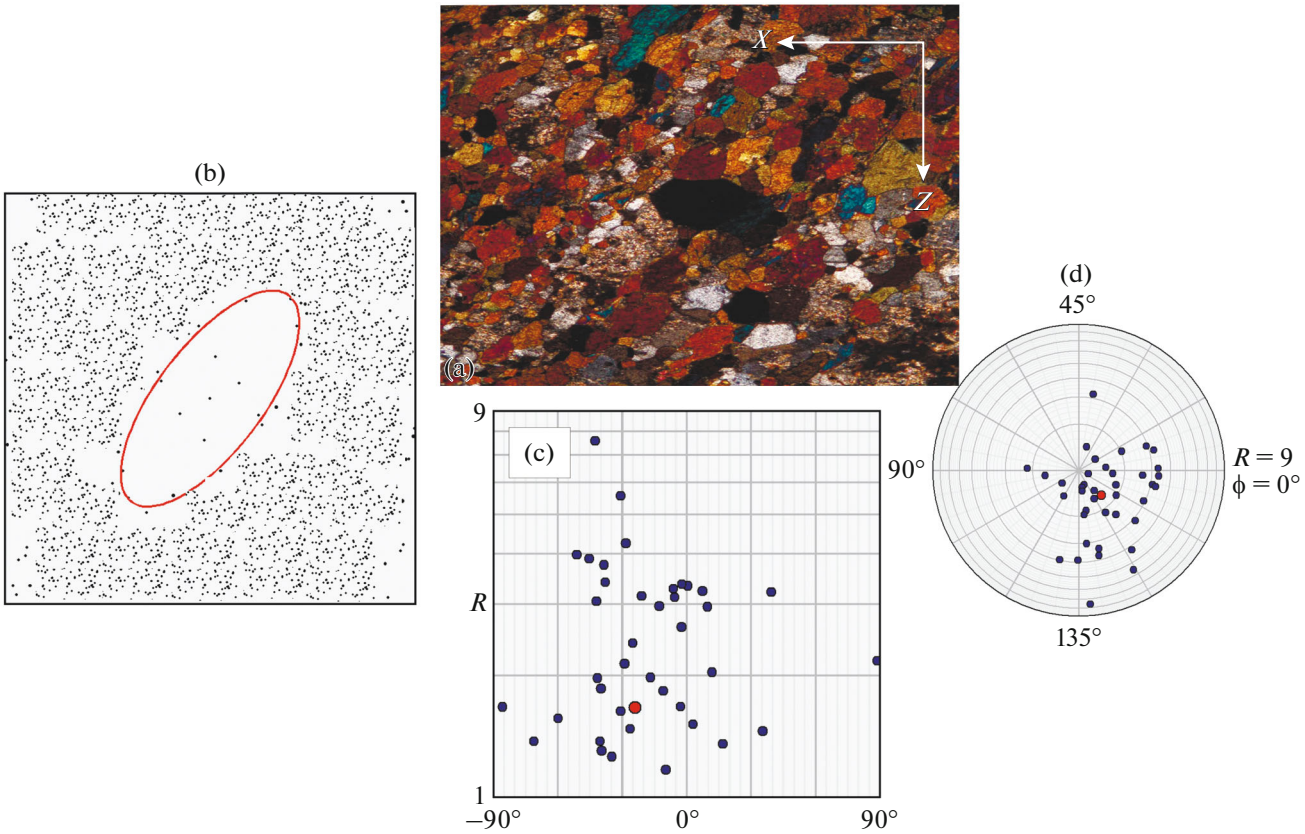

Fig. 8. Finite strain graphs for sample S39-1: (a) orientation of the X and Z axes in the thin section, (b) center to center graph, (c) Rf/phi graph, (d) polar graph.

(Table 1). The axial ratios (XZ) range from 1.50 to 4.46 and S_X ranges from 1.16 to 2.37 for the Fry technique (Fig. 10). The stretches in the Z direction (S_Z) range from 0.40 to 0.70, displaying vertical shortening of 30% to 60% calculated by R_f/ϕ method and about 0.48 to 0.83, showing vertical shortening of 17 to 52% for Fry method. S_Y ranges from 0.70 to 1.46 revealing contraction and extension. Estimations of the deformation grade made in the field and calculated in thin sections have the same order in the different lithologies. Figure 11a, b show that the strain symmetry (K) and the strain ellipsoids are more prolate and show the change in stretches Sx and Sy [15]. Our data indicate that the stretch (Sx) increased and the stretch (S_Y) decreased with strain symmetry (K). S_Z displays no

Table 1. Direction of finite strain axes and stretches for samples from um Junud area

Sample	Rock types	Method	Rx	Ry	X	Y	Z	XY	YZ	XZ	K	r	logXY	logZY	Nadai	Lodi
S 3-1	Amphibolite	Fry	2.53	2.35	1.4	1.3	0.55	1.08	2.35	2.53	0.06	2.43	0.03	–0.37	0.73	0.841
		$R_{f/\varphi}$	2.7	1.75	1.61	1.04	0.6	1.54	1.75	2.7	0.72	2.29	0.19	–0.24	0.704	0.127
S 3-2	Amphibolite	Fry	3.92	1.16	2.37	0.7	0.6	3.38	1.16	3.92	14.87	3.54	0.53	–0.06	1.06	0.783
		$R_{f/\varphi}$	1.75	1.69	1.22	1.18	0.7	1.04	1.69	1.75	0.05	1.73	0.02	–0.23	0.443	0.875
S 4-1	Granitic gneiss	Fry	1.82	1.53	1.29	1.09	0.71	1.19	1.53	1.82	0.36	1.72	0.08	–0.18	0.436	0.42
		$R_{f/\varphi}$	1.74	1.68	1.22	1.17	0.7	1.04	1.68	1.74	0.05	1.72	0.02	–0.23	0.439	0.873
S11-1	Gneiss	Fry	2.8	1.73	1.65	1.02	0.59	1.62	1.73	2.8	0.85	2.35	0.21	–0.24	0.729	0.065
		$R_{f/\varphi}$	2.17	2.12	1.3	1.27	0.6	1.02	2.12	2.17	0.02	2.14	0.01	–0.33	0.623	0.94
S11-2	Gneiss	Fry	2.93	1.42	1.82	0.88	0.62	2.06	1.42	2.93	2.53	2.48	0.31	–0.15	0.775	0.348
		$R_{f/\varphi}$	2.15	1.85	1.36	1.17	0.63	1.16	1.85	2.15	0.19	2.01	0.07	–0.27	0.574	0.607
S12-1	Granite	Fry	2.42	1.98	1.44	1.17	0.59	1.22	1.98	2.42	0.23	2.2	0.09	–0.3	0.655	0.546
		$R_{f/\varphi}$	1.84	1.82	1.23	1.22	0.67	1.01	1.82	1.84	0.01	1.83	0	–0.26	0.493	0.964
S13-1	Amphibolite	Fry	2.99	1.42	1.85	0.88	0.62	2.11	1.42	2.99	2.63	2.53	0.32	–0.15	0.791	0.36
		$R_{f/\varphi}$	4.37	3.45	1.77	1.4	0.4	1.27	3.45	4.37	0.11	3.72	0.01	–0.54	1.12	0.679
S13-2	Amphibolite	Fry	1.63	1.35	1.25	1.04	0.77	1.21	1.35	1.63	0.59	1.56	0.08	–0.13	0.348	0.228
		$R_{f/\varphi}$	3.51	3.32	1.55	1.46	0.44	1.06	3.32	3.51	0.02	3.38	0.02	–0.52	1.003	0.911
S15-1	Amphibolite	Fry	1.5	1.45	1.16	1.12	0.77	1.03	1.45	1.5	0.08	1.48	0.01	–0.16	0.318	0.833
		$R_{f/\varphi}$	2	1.99	1.26	1.26	0.63	1.01	1.99	2	0.01	2	0	–0.03	0.564	0.986
S16-1	Granite	Fry	1.7	1.39	1.28	1.04	0.75	1.22	1.39	1.7	0.57	1.61	0.09	–0.14	0.379	0.241
		$R_{f/\varphi}$	1.87	1.79	1.25	1.2	0.67	1.04	1.79	1.87	0.06	1.83	0.02	–0.25	0.494	0.86
S17-1	Amphibolite	Fry	2.6	2.1	1.48	1.19	0.57	1.24	2.1	2.6	0.22	2.34	0.09	–0.32	0.709	0.553
		$R_{f/\varphi}$	2.99	2.84	1.47	1.39	0.49	1.05	2.84	2.99	0.03	2.89	0.02	–0.45	0.874	0.906
S17-2	Amphibolite	Fry	2.4	1.76	1.48	1.09	0.62	1.36	1.76	2.4	0.48	2.12	0.13	–0.25	0.628	0.291
		$R_{f/\varphi}$	2.84	2.62	1.45	1.34	0.51	1.08	2.62	2.84	0.05	2.7	0.04	0.42	0.821	0.846
S18-1	Amphibolite	Fry	3.14	1.63	1.82	0.95	0.58	1.93	1.63	3.14	1.47	2.56	0.28	–0.21	0.812	–0.146
		$R_{f/\varphi}$	2.61	1.77	1.57	1.06	0.06	1.47	1.77	2.61	0.62	2.24	0.17	–0.25	0.682	0.19
S21-1	Amphibolite	Fry	2.71	2.18	1.5	1.21	0.55	1.24	2.18	2.71	0.21	2.42	0.09	–0.34	0.741	0.536
		$R_{f/\varphi}$	3.3	2.3	1.68	1.17	0.51	1.43	2.3	3.3	0.33	2.73	0.16	–0.36	0.866	0.395
S34-1	Amphibolite	Fry	3.03	2.47	1.55	1.26	0.51	1.23	2.47	3.03	0.15	2.7	0.09	–0.39	0.834	0.631
		$R_{f/\varphi}$	3	2.6	1.51	1.31	0.5	1.15	2.6	3	0.1	2.75	0.06	–0.41	0.845	0.739
S34-2	Amphibolite	Fry	2.47	1.71	1.53	1.06	0.62	1.44	1.71	2.47	0.63	2.15	0.16	–0.23	0.643	0.187
		$R_{f/\varphi}$	2.88	2.46	1.5	1.28	0.52	1.17	2.46	2.88	0.12	2.63	0.07	–0.39	0.807	0.702
S34-3	Amphibolite	Fry	2.33	1.69	1.48	1.07	0.63	1.38	1.69	2.33	0.55	2.07	0.14	–0.23	0.604	0.241
		$R_{f/\varphi}$	2.79	2.44	1.47	1.29	0.53	1.14	2.44	2.79	0.1	2.58	0.06	–0.39	0.789	0.739
S34-4	Amphibolite	Fry	2.18	1.51	1.47	1.02	0.67	1.44	1.51	2.18	0.87	1.95	0.16	–0.18	0.551	0.058
		$R_{f/\varphi}$	2.73	2.39	1.46	1.28	0.54	1.14	2.39	2.73	0.1	2.53	0.06	–0.38	0.771	0.735
S34-5	Amphibolite	Fry	1.98	1.49	1.38	1.04	0.7	1.33	1.49	1.98	0.67	1.82	0.12	–0.17	0.485	0.168
		$R_{f/\varphi}$	2.65	2.22	1.47	1.23	0.55	1.19	2.22	2.65	0.16	2.41	0.08	–0.35	0.734	0.637
S35-1	Hornblend Quartz schist	Fry	4.46	1.77	2.24	0.89	0.5	2.52	1.77	4.46	1.97	3.29	0.4	–0.025	1.067	–0.236
		$R_{f/\varphi}$	2.21	2.04	1.34	1.23	0.61	1.08	2.04	2.21	0.08	2.12	0.03	–0.31	0.617	0.798
S35-2	Hornblend Quartz schist	Fry	4.15	1.47	2.27	0.8	0.55	2.82	1.47	4.15	3.88	3.29	0.45	–0.17	1.041	–0.459
		$R_{f/\varphi}$	2.12	2.03	1.3	1.25	0.61	1.04	2.03	2.12	0.04	2.07	0.02	–0.31	0.597	0.885

Table 1. (Contd.)

Sample	Rock types	Method	Rx	Ry	X	Y	Z	XY	YZ	XZ	K	r	logXY	logZY	Nadai	Lodi
S35-3	Hornblend Quartz schist	Fry	3.17	1.34	1.96	0.83	0.62	2.37	1.34	3.17	4.02	2.71	0.37	–0.13	0.848	–0.493
		$R_{f/\varphi}$	2.11	2.01	1.3	1.24	0.62	1.05	2.01	2.11	0.05	2.06	0.02	–0.03	0.591	0.87
S35-4	Hornblend Quartz schist	Fry	3.16	1.22	2.02	0.78	0.64	2.59	1.22	3.16	7.23	2.81	0.41	–0.09	0.87	–0.654
		$R_{f/\varphi}$	2.06	1.98	1.29	1.24	0.63	1.04	1.98	2.06	0.04	2.02	0.02	–0.3	0.575	0.89
S35-5	Hornblend Quartz schist	Fry	2.34	1.06	1.73	0.78	0.74	2.21	1.06	2.34	20.13	2.27	0.34	–0.03	0.672	0.863
		$R_{f/\varphi}$	2.04	1.87	1.31	1.2	0.64	1.09	1.87	2.04	0.1	1.96	0.04	–0.27	0.55	0.756
S35-6	Hornblend Quartz schist	Fry	2.25	1.05	1.69	0.79	0.75	2.14	1.05	2.25	22.86	2.19	0.33	–0.02	0.643	–0.88
		$R_{f/\varphi}$	2.04	1.83	1.32	1.18	0.64	1.11	1.83	2.04	0.14	1.94	0.05	–0.26	0.543	0.695
S37-1	Amphibolite	Fry	2.84	1.48	1.76	0.92	0.62	1.92	1.48	2.84	1.91	2.4	0.28	–0.17	0.746	–0.249
		$R_{f/\varphi}$	1.99	1.89	1.28	1.22	0.64	1.05	1.89	1.99	0.06	1.94	0.02	–0.28	0.542	0.85
S37-2	Amphibolite	Fry	2.11	1.37	1.48	0.96	0.7	1.54	1.37	2.11	1.46	1.91	0.19	–0.14	0.53	–0.157
		$R_{f/\varphi}$	1.97	1.87	1.28	1.21	0.65	1.05	1.87	1.97	0.06	1.92	0.02	–0.27	0.534	0.846
S37-3	Amphibolite	Fry	1.54	1.13	1.28	0.94	0.83	1.36	1.13	1.54	2.79	1.49	0.13	–0.05	0.315	–0.434
		$R_{f/\varphi}$	1.94	1.84	1.27	1.2	0.65	1.05	1.84	1.94	0.06	1.89	0.02	–0.26	0.521	0.84
S39-1	Amphibolite	Fry	2.77	2.13	1.53	1.18	0.55	1.3	2.13	2.77	0.27	2.43	0.11	–0.33	0.748	0.484
		$R_{f/\varphi}$	2.72	2.34	1.47	1.26	0.54	1.16	2.34	2.72	0.12	2.5	0.07	–0.37	0.763	0.699
S39-2	Amphibolite	Fry	2.7	1.94	1.55	1.12	0.58	1.39	1.94	2.7	0.42	2.33	0.14	–0.29	0.715	0.334
		$R_{f/\varphi}$	2.69	2.34	1.46	1.27	0.54	1.15	2.34	2.69	0.11	2.49	0.06	–0.37	0.757	0.718
S39-3	Amphibolite	Fry	2.33	1.93	1.41	1.17	0.61	1.21	1.93	2.33	0.22	2.14	0.08	–0.29	0.628	0.555
		$R_{f/\varphi}$	2.38	2.31	1.35	1.31	0.57	1.03	2.31	2.38	0.02	2.34	0.01	–0.36	0.696	0.931
S39-4	Amphibolite	Fry	2.3	1.83	1.42	1.13	0.62	1.26	1.83	2.3	0.31	2.09	0.1	–0.26	0.609	0.451
		$R_{f/\varphi}$	2.36	2.24	1.35	1.29	0.57	1.05	2.24	2.36	0.04	2.29	0.02	–0.35	0.681	0.878
S40-1	Amphibolite	Fry	3.87	2.39	1.84	1.14	0.48	1.62	2.39	3.87	0.45	3.01	0.21	–0.38	0.97	0.288
		$R_{f/\varphi}$	2.95	2.58	1.5	1.31	0.51	1.14	2.58	2.95	0.09	2.72	0.06	–0.41	0.834	0.752
S40-2	Amphibolite	Fry	3.52	1.68	1.95	0.93	0.55	2.1	1.68	3.52	1.61	2.78	0.32	–0.23	0.894	0.176
		$R_{f/\varphi}$	2.93	2.56	1.5	1.31	0.51	1.14	2.56	2.93	0.09	2.7	0.06	–0.41	0.828	0.749
S67-1	Sheared Granite	Fry	3.83	2.38	1.83	1.14	0.48	1.61	2.38	3.83	0.44	2.99	0.21	–0.38	0.963	0.291
		$R_{f/\varphi}$	1.87	1.75	1.26	1.18	0.67	1.07	1.75	1.87	0.09	1.82	0.03	–0.24	0.486	0.788
S67-2	Sheared Granite	Fry	2.86	1.16	1.92	0.78	0.67	2.47	1.16	2.86	9.16	2.63	0.39	–0.06	0.804	0.718
		$R_{f/\varphi}$	1.75	1.67	1.22	1.17	0.7	1.05	1.67	1.75	0.07	1.72	0.02	–0.22	0.439	0.833

correlation between strain value (K) and vertical shortening (Fig. 11c). The strain analysis depends on the three principal stretches, which can indicate the positive and negative correlations for S_X and S_Y related to the K value. In other case, the correlation between strain magnitude (E_t) and strain value K is not identified in the regional maps.

DISCUSSION

The Neoproterozoic evolution of the Arabian-Nubian Shield (ANS) has been the subject matter of detailed discussions in many published works. The ANS tectonic evolution is traditionally subdivided into two main orogenic stages.

(1) The first stage occured from ca. 870 Ma to 650 Ma and was well developed in belts with oceanic affinity. [33] suggested that the sequence of tectonic events was started by the sea-floor spreading and formation of forarc and back-arc basins and followed by the accretion of these cells into juvenile crust.

(2) The second stage happened between 650 Ma to 550 Ma and was characterized by belts of continental affinity. In the second stage, metamorphism and deformation occurred 650–620 Ma ago and characterize as a feasible collisional stage through the accumulated Pan-African terranes accreted to the East

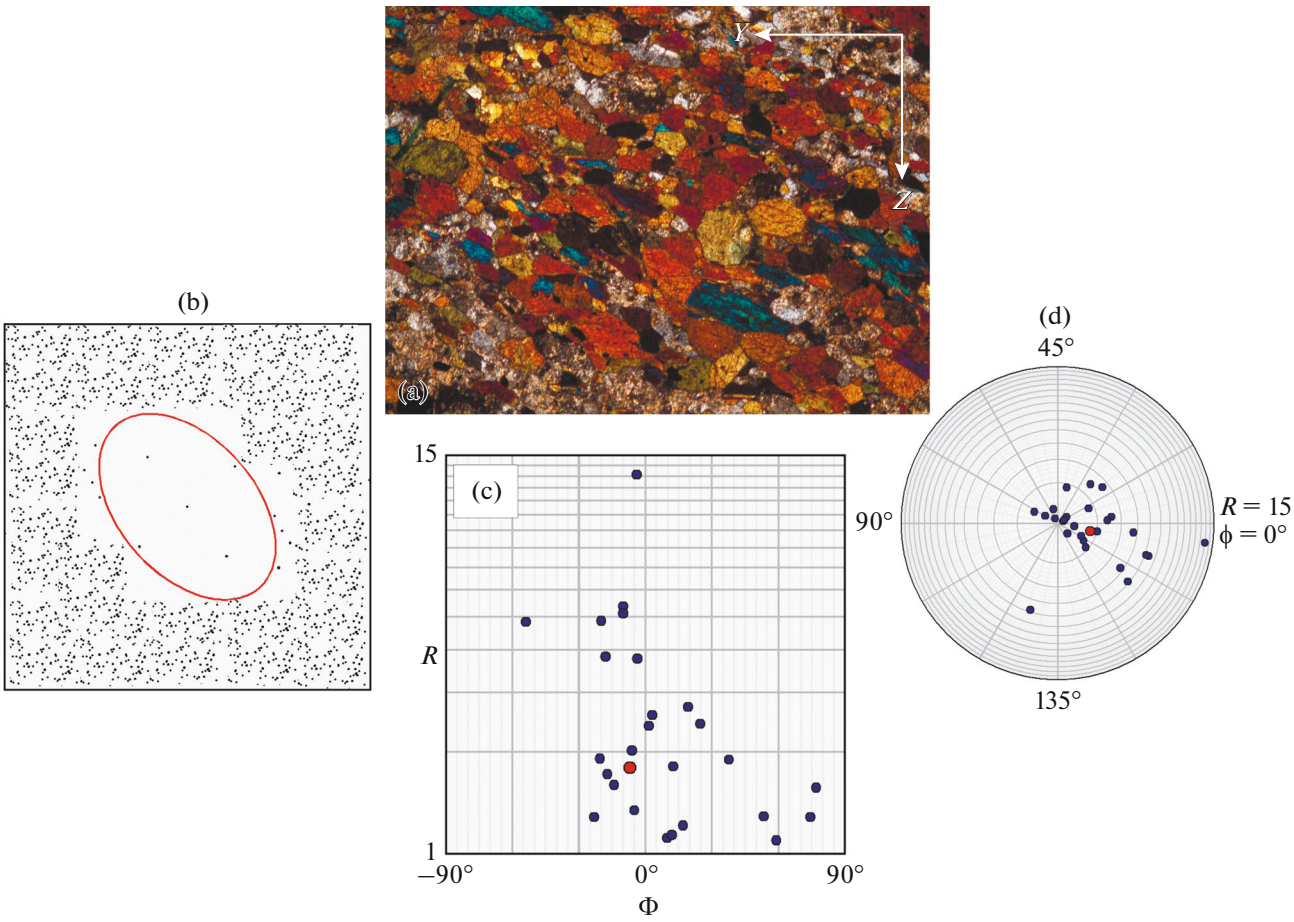

Fig. 9. Finite strain graphs for sample S39-1: (a) orientation of the Y and Z axes in the thin section, (b) center to center graph, (c) Rf/phi graph, (d) polar graph.

Saharan Craton (ESC) [30, 35]. R.Stern [33] believed that the collision event was contemporary with the collision between East and West Gondwanalands. Many authors think that the extension is followed at the Neoproterozoic-Cambrian boundary by the collision in the ANS and was concomitant with early breakup of the continent of Gondwana [33, 8, 11]. For example, the Najd Fault System formed 630–540 Ma ago during an extensional phase [34, 36].

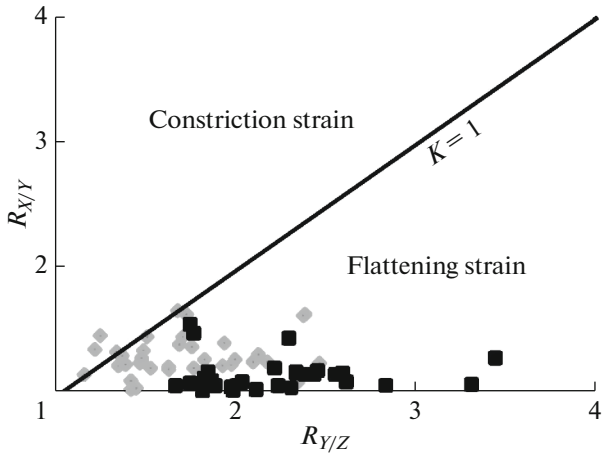

Fig. 10. Flinn diagram [10] showing relative strain or strain ellipsoid shape as obtained from twenty samples by the R_f/ϕ method (gray square) and Fry method (black square).

In the present study, the obtained data show that the granitic gneiss, hornblende schist and amphibolite were thrusted from the WNW to the ESE trend. The lineations in the studied area trend W to WNW during thrusting and are related to kinematic indicators enrollment WNW tectonic transport. In this case, we argue that the tectonic setting resulted in conditions that favoured the developmant of the subhorizontal main-phase foliation that is parallel to subparallel to the contact for granitic gneiss, hornblende schist and amphibolite rocks in the entire Um Junud region. The axial ratios in XZ sections indicate low to medium values in the various lithologic units of the Junud area. We consider that the ductile strain characterized by the varying XZ axial ratios (up to ~10) was superimposed heterogeneously on the current nappe structure [21]. Furthermore, in the present area, we suggest the considerable movement at the bounding faults, at least in part, before the high strain accumulation.

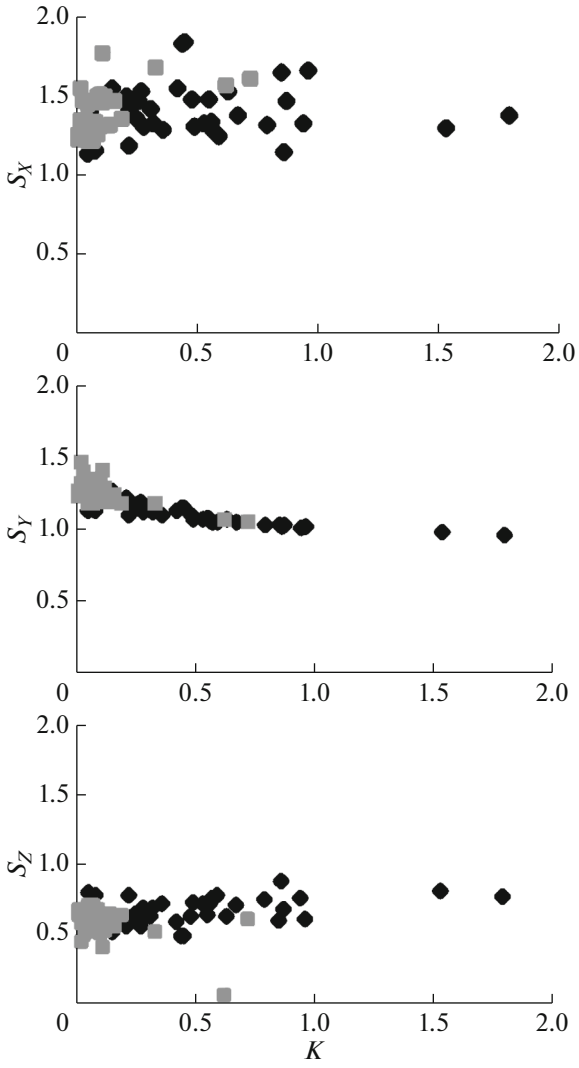

Fig. 11. Flinn diagram [10] showing relative strain or strain ellipsoid shape as obtained by the R_f/ϕ method (gray Square) and Fry method (black rhomb). (a) S_X vs K showing positive correlation, (b) S_Y vs K showing pronounced negative correlation, (c) S_Z vs K depicting no obvious correlation.

During the regional thrusting event documented in the vicinity of the Junud area, low grade rocks similar to those dominating the present area were thrusted and themselves were deformed by minor local thrusts. Thus, the presence of pre-high-pressure tectonics near to the contacts of nappes was valuable due to the nappes formed during thrusting by brittle imbrication. This indicates that extremely heterogeneous strain affected the pre-existing structures in the greater extent and some domains in and between shear zones in a lesser extent. The strain type in the present work which is expressed by the strain ellipsoid shape (K value) does not display any distinct pattern in the area. Also, the K value suggests that the thrusting was associated with vertical shortening and it displays the flattening strain type in large parts of the concerned area. Thus, we suggest that the nappe contacts were shaped during a progressive overthrusting under semi-brittle to semi-ductile conditions predating metamorphism.

Our conclusion is in harmony with that given by [21] that in the high-grade metamorphic rocks, minor or no volume changes was detected due to the porosities remain very low during deformation. The strain data show that the majority are of oblate strain and a few indicate prolate strain in the Um Junud region. In this work, we suggest that the vertical shortening played its role by pure shearing and the simple shearing during thrusting with accumulation of ductile deformation. It is concluded that the vertical shortening resulted to the subhorizontal foliation in the studied area. In other words, pure shear was related to the vertical shortening and produced the subhorizontal foliation in the studied locality [28, 19, 6]. R. Law [23] explained that the shearing conditions which were represented by pure and/or simple shear components, have a non-linear relationship and create the same contributions to the overall deformation at Wm = 0.71. The average kinematic vorticity is 0.5–0.6 as is suggested by the fabric skeleton of quartz c-axis fabrics [23]. These averages show a pure shear-dominated bulk deformation during nappe emplacement which is thus characterized by dominating of the ductile nappe-emplacement-related deformation.

CONCLUSIONS

The main concluding remarks obtained from the microstructural investigation and quantitative strain analysis of the deformed lithologies outcropping at the Um Jund area are the next.

(1) The finite strain determined in the majority of the studied samples is characterized by the oblate shape of the strain ellipsoid; the prolate shape was established only in several samples.

(2) The principal strain axes displays a clustering along N-WNW trend, and shallow WNW plunging in the majority of the studied samples.

(3) The strain magnitude has the same order in various lithologic units and formed under semi-brittle to semi-ductile conditions.

(4) According to the microstructural analysis data, ductile strain accumulated during thrusting.

ACKNOWLEDGMENTS

The authors would like to extend their sincere appreciation to the Deanship of Scientific Research at King Saud University for funding this research through the Research Group Project no. RGP-VPP-230. We thank journal reviewers for critical and helpful comments and for editorial handling.

REFERENCES

1. M. A. Abd El-Wahed, "Pan-African strike-slip tectonics of Wadi El-Dabbah area, north Sibai Core Complex, Central Eastern Desert, Egypt," Ann. Egypt. Geol. Surv. **29**, 1–36 (2007).
2. M. A. Abd El-Wahed, "Thrusting and transpressional shearing in the Pan-African nappe southwest El-Sibai core complex, Central Eastern Desert, Egypt," J. Afr. Earth Sci. **50**, 16–36 (2008).
3. M. A. Abd El-Wahed and M. Abu Anbar, "Synoblique convergent and extensional deformation and metamorphism in the Neoproterozoic rocks along Wadi Fatira shear zone, Northern Eastern Desert, Egypt," Arab. J. Geosci. **2**, 29–52 (2009).
4. M. G. Abdelsalam, M. M. Abdeen, H. M. Dowidar, R. J. Stern, and A. A. Abdelghaffar, "Structural evolution of the Neoproterozoic western Allaqi-Heiani Suture Zone, Southern Egypt," Precambrian Res. **124**, 87–104 (2003).
5. M. Al Shanti and M. J. Roobol, "A late Proterozoic ophiolite complex at Jabal Ess in northern Saudi Arabia," Nature **279**, 488–491 (1979).
6. A. M. Al-Saleh and O. M. K. Kassem, "Microstructural strain analysis and $^{40}Ar/^{39}Ar$ evidence for the origin of the Mizil gneiss dome, eastern Arabian Shield, Saudi Arabia," J. Afr. Earth Sci. **70**, 24–35 (2012).
7. A. R. Bakor, I. G. Gass, and C. R. Neary, "Jabal al Wask, northwest Saudi Arabia: an Eocambrian back-arc ophiolite," Earth Planet. Sci. Lett. **30**, 1–9 (1976).
8. B. Blasband, S. White, P. Brooijmans, H. De Boorder, and W. Visser, "Late Proterozoic extensional collapse in the Arabian–Nubian Shield," J. Geol. Soc. (London, U. K.) **157**, 615–628 (2000).
9. S. El Gaby, F. K. List, and R. Tehrani, "The basement complex of the Eastern Desert and Sinai," in *The Geology of Egypt*, Ed. by R. Said (Balkema, Rotterdam, 1990), pp. 175–184.
10. D. Flinn, "On folding during three-dimensional progressive deformation," Q. J. Geol. Soc. London **118**, 385–433 (1962).
11. H. Fritz, D. R. Dallmeyer, E. Wallberecher, J. Loizenbauer, G. Hoinkes, P. Neumayr, and A. A. Khudeir, "Neoproterozoic tectonothermal evolution of the central Eastern Desert, Egypt; a slow velocity tectonic process of core complex exhumation," J. Afr. Earth Sci. **34**, 137–155 (2002).
12. H. Fritz, E. Wallbrecher, A. A. Khudier, F. A. El Ela, and R. D. Dallmeyer, "Formation of Neoproterozoic metamorphic core complexes during oblique convergence, eastern Desert, Egypt," J. Afr. Earth Sci. **23**, 311–329 (1996).
13. M. S. Garson, and I. M. Shalaby, "Precambrian–Lower Paleozoic plate tectonics and metallogenesis in the Red Sea region," Geol. Assoc. Can., Spec. Pap. **14**, 573–596 (1976).
14. I. G. Gass, "Upper Proterozoic (Pan-African) calc-alkaline magmatism in northeastern Africa and Arabia," in *Andesites*, Ed. by R. S. Thorpe (Wiley, New York, 1982), pp. 591–609.
15. J. R. Hossack, "Pebble deformation and thrusting in the Bygdin area, Southern Norway," Tectonophysics **5**, 315–339 (1968).
16. I. M. Hussein, A. Kröner, and S. Durr, "Wadi Onib—a dismembered Pan-African ophiolite in the Red Sea Hills of Sudan," Bull. Fac. Earth Sci., King Abdul aziz Univ., Jeddah. **6**, 320–327 (1984).
17. O. M. K. Kassem, "Kinematic analysis of the Migif area in the Eastern Desert of Egypt," J. Afr. Earth Sci. **90**, 136–149 (2014).
18. O. M. K. Kassem, "Strain analysis and deformation in the Tanumah Area, Arabian Shield, Saudi Arabia," Arab. J. Geosci. **8**, 4127–4138 (2015).
19. O. M. K. Kassem, "Strain analysis and heterogeneous deformation in the Migif area, Eastern Desert, Egypt," Ann. Egypt. Geol. Surv. **30**, 103–119 (2008).
20. O. M. K. Kassem and S. H. Abdel Raheim, "Finite-strain analysis of Metavolcano-sedimentary rocks at Gabel El Mayet area, Central Eastern Desert, Egypt," J. Afr. Earth Sci. **58**, 321–330 (2010).
21. O. M. K. Kassem and U. Ring, "Underplating-related finite-strain patterns in the Gran Paradiso massif, Western Alps, Italy: heterogeneous ductile strain superimposed on a nappe stack," J. Geol. Soc. (London, U.K.) **161**, 875–884 (2004).
22. A. Kröner, J. Krüger, and A. A. Rashwan, "Age and tectonic setting of granitoid gneisses in the Eastern Desert of Egypt and south-west Sinai," Geol. Rundsch. **83**, 502–513 (1994).
23. R. D. Law, M. P. Searle, and R. L. Simpson, "Strain, deformation temperatures and velocity of flow at the top of the Greater Himalayan Slab, Everest Massif, Tibet," J. Geol. Soc. (London, U.K.) **161**, 305–320 (2004).
24. J. Loizenbauer, E. Wallbrecher, H. Fritz, P. Neumayr, A. A. Khudeir, and U. Kloetzli, "Structural geology, single zircon ages and fluid inclusion studies of the Meatiq metamorphic core comple: Implications for Neoproterozoic tectonics in the Eastern Desert of Egypt," Precambrian Res. **110**, 357–383 (2001).
25. W. H. Owens, "The calculation of a best-fit ellipsoid from elliptical sections on arbitrarily oriented planes," J. Struct. Geol. **6**, 571-578 (1984).
26. C. W. Passchier and R. A. Trouw, *Microtectonics* (Springer, Berlin, 1995).
27. C. J. Peach and R. J. Lisle, "A Fortran IV program for the analysis of tectonic strain using deformed elliptical markers." Comput. Geosci. **5**, 325–334 (1979).
28. U. Ring and O. M. K. Kassem, "The nappe rule: why does it work?," J. Geol. Soc. (London, U.K.) **164**, 1109–1112 (2007).
29. H. Schandelmeier, D. P. F. Darbyshire, U. Harms, and A. Richter, "The East Sahara Craton: evidence for pre-Pan-African crust in NE Africa west of the Nile," in *The Pan-African Belt of NE Africa and Adjacent Areas*, Ed. by S. El Gaby and R. O. Greiling (Vieweg, Braunschweig, 1988), pp. 69–94.
30. H. Schandelmeier, A. Richter, and U. Harms, "Proterozoic deformation of the East Sahara Craton in

southeast Libya, south Egypt and north Sudan," Tectonophysics **140**, 233–246 (1987).

31. R. M. Shackleton, A. C. Ries, R. H. Graham, and W. R. Fitches, "Late Precambrian ophiolitic mélange in the Eastern Desert of Egypt," Nature **285**, 472–474 (1980).
32. C. Simpson and D. G. De Poar, "Strain and kinematic analysis in general shear zones," J. Struct. Geol. **15**, 1–20 (1993).
33. R. J. Stern, "Neoproterozoic (900–550 Ma) arc assembly and continental collision in the East African orogeny: implications for the consolidation of Gondwanaland," Annu. Rev. Earth Planet. Sci. **22**, 319–351 (1994).
34. R. J. Stern and C. E. Hedge, "Geochronologic and isotopic constraints on Late Precambrian crustal evolution in the Eastern Desert of Egypt," Am. J. Sci. **285**, 97–127 (1985).
35. M. Sultan, R. D. Tucker, Z. El Alfy, R. Attia, and A. G. Ragab, "U–Pb (zircon) ages for the gneissic terrane west of the Nile, southern Egypt," Geol. Rundsch. **83**, 514–522 (1994).
36. M. Sultana, R. D. Tucker, R. I. Gharbawi, A. I. Ragab, and Z. El Alfy, "On the location of the boundary between the Nubian Shield and the old African continent: Inferences from U–Pb (zircon) and common Pb data," in *Geoscientific Research in Northeast Africa*, Ed. by U. Thorweihe and H. Schandelmeier (Balkema, Rotterdam, 1993), pp. 75–77.
37. E. Wallbrecher, H. Fritz, A. A. Khudeir, and F. Farahat, "Kinematics of Pan-African thrusting and extension in Egypt," in *Geoscientific Research in Northeast Africa*, Ed. by U. Thorweihe and H. Schandelmeier (Balkema, Rotterdam, 1993), pp. 27–30.

Reviewer: V. V. Balagansky